

A Weak Lensing Detection of the Cosmological Distance-Redshift Relation Behind Three Massive Clusters^{*}

Elinor Medezinski¹, Tom Broadhurst^{2,3}, Keiichi Umetsu⁴, Narciso Benítez⁵
& Andy Taylor⁶

¹*Department of Physics & Astronomy, The Johns Hopkins University, 3400 N. Charles Street, Baltimore, MD 21218, USA*

²*Theoretical physics, University of the Basque Country, Bilbao 48080, Spain*

³*Ikerbasque, Basque Foundation for Science, Alameda Urquijo, 36-5 Plaza Bizkaia 48011, Bilbao, Spain*

⁴*Institute of Astronomy and Astrophysics, Academia Sinica, P. O. Box 23-141, Taipei 106, Taiwan, Republic of China*

⁵*Instituto de Astrofísica de Andalucía (CSIC), Granada, Spain*

⁶*Scottish Universities Physics Alliance (SUPA), Institute for Astronomy, School of Physics, University of Edinburgh, Royal Observatory, Blackford Hill, Edinburgh, EH9 3HJ, U.K.*

24 October 2018

ABSTRACT

The amplitude of weak lensing should increase with source distance, rising steeply behind a lens and saturating at high redshift, providing a model-independent means of measuring cosmic geometry. We measure the amplitude of weak lensing with redshift for three massive clusters, A370 ($z = 0.375$), ZwCl0024+17 ($z = 0.395$) and RXJ1347-11 ($z = 0.451$), using deep, three-colour Subaru imaging. We define the depth of lensed populations with reference to the COSMOS and GOODS fields, providing a consistency check of photo- z estimates over a wide range of redshift and magnitude. The predicted distance-redshift relation is followed well for the deepest dataset, A370, for a wide range of cosmologies, and is consistent with less accurate data for the other two clusters. Scaling this result to a new survey of ~ 25 massive clusters should provide a useful cosmological constraint on w , complementing existing techniques, with distance measurements covering the untested redshift range, $1 < z < 5$.

Key words: cosmology: observations – gravitational lensing – galaxies: clusters: individual(Abell 370) – galaxies: clusters: individual(ZwCl 0024.0+1652) – galaxies: clusters: individual(RX J1347.5-1145)

1 INTRODUCTION

Constraining cosmological parameters has been the focus of major surveys in the last decade, via precision cosmic microwave background (CMB) temperature correlations (Spergel et al. 2007; Brown et al. 2009) and SN-Ia light curves (Riess et al. 1998; Perlmutter et al. 1999). A standard, Λ CDM, cosmological model has been defined by this work, albeit at the price of accepting an accelerating expansion driven by a cosmological constant, and non-baryonic dark matter (DM) of an unknown nature dominating the mass density of the Universe. Measurements of the angular diameter distance of the CMB refer to $z \sim 1100$, and luminosity distances are derived from SN-Ia in the range $z < 1$.

In principle, lensing can provide a complementary distance measurements in the range, $z > 1$, from the purely geometric deflection of light, which increases with source distance behind a lens.

For lensing clusters, the bend-angle of light scales linearly with angular diameter distance ratio, d_{ls}/d_s , the separation between the lens and the source, divided by distance to the source. This distance ratio has a characteristic geometric dependence on redshift, rising steeply behind the lens and then saturating at large source redshift (e.g., Fig. 1 of Broadhurst, Taylor & Peacock 1995). This effect has been detected behind massive lensing clusters, where the separation in angle between multiple images of higher redshift sources is noticeably larger than for lower redshift sources. For example, for the well studied cluster SDSSJ1004+4112 ($z = 0.68$), five images of a QSO at $z = 1.734$ are within an Einstein radius of about $\theta_E \sim 7''$ (Inada et al. 2003; Oguri et al. 2004), whereas a more distant multiply lensed

^{*} Based on data collected at Subaru Telescope and obtained from the SMOKA, which is operated by the Astronomy Data Center, National Astronomical Observatory of Japan.

galaxy behind this cluster at $z = 3.332$ is at a much larger Einstein radius of $\theta_E \sim 16''$ (Sharon et al. 2005). Other sets of multiple images show this increasing angular scaling with source redshift, following well the expected general form of the redshift-distance relation in careful strong lensing analyses of deep Hubble data (Soucail, Kneib & Golse 2004; Broadhurst et al. 2005; Zitrin et al. 2009b; Zitrin & Broadhurst 2009; Zitrin et al. 2009a).

However, these studies are not able to distinguish between the relatively subtle changes between cosmologies in the range of interest, due to the inherent insensitivity of the distance ratio d_{ls}/d_s to the cosmological parameters. Moreover, the bend-angle is particularly sensitive to the gradient of the mass profile, requiring many sets of multiple images in the strong regime to simultaneously solve for both the cosmological model and the mass distribution. Instead in practice, strong lens modeling usually adopts the standard cosmological relation in order to better derive the mass distribution, with multiply lensed sources forced to lie on the lensing distance-redshift relation. This helps eliminate the otherwise considerable degeneracy in constraining the slope of the lensing mass profile of a galaxy cluster (Broadhurst et al. 2005; Zitrin et al. 2009b; Zitrin & Broadhurst 2009; Zitrin et al. 2009a). The hope of constraining the cosmography from strong lensing data is remote with current tools (Gillmore & Natarajan 2009).

Weak lensing (WL), by contrast, offers a model independent way of constraining the cosmological parameters via the distance-redshift relation (Taylor et al. 2004). Image distortions and magnification depend on gradients of the deflection field and in the WL limit, these are just proportional to d_{ls}/d_s . The mass profile enters only in the stronger regime as a second order correction (Medezinski et al. 2007). Here we are concerned with the amplitude of cluster WL dependence on source redshift, for which no mass reconstruction is required when evaluating the distance-redshift relation. However, although this observed effect is independent of the mass distribution in the weak limit, the sensitivity to cosmological parameters is still inherently very small.

The analogous effect in the field has been explored in terms of the cosmic shear, to measure the general mass distribution. Optimal formalisms have been developed which cross-correlate the foreground distribution of galaxies along a given line of sight with the distribution of background images (Wittman et al. 2001; Jain & Taylor 2003; Bacon et al. 2003; Taylor et al. 2004, 2007) with clear detections of large scale structure, including the COMBO-17 fields (Brown et al. 2003; Kitching et al. 2007) and the COSMOS field (Massey et al. 2007; Schrabback et al. 2010). To usefully derive cosmological parameters from general cosmic shear work, deep all-sky surveys have been proposed (e.g., LSST¹, DES², JDEM³, EUCLID⁴).

Here we make use of detailed colour-colour (CC) information for three intermediate redshift lensing clusters, A370 ($z = 0.375$), ZwCl0024+17 ($z = 0.395$), RXJ1347-11 ($z = 0.451$) and define several samples of galaxies of differing

Table 1. The Cluster Sample: Redshift and Filter Information

Cluster	z	Filters used ¹ (exp' time in sec)	Seeing (arcsec)
A370	0.375	$B_J(7200)$, $R_C(8340)$, $z'(14221)$	0.6
ZwCl0024+17	0.395	$B_J(3600)$, $R_C(5280)$, $z'(1680)$	0.8
RXJ1347-11	0.451	$V_J(1800)$, $R_C(2880)$, $z'(4860)$	0.76

¹Detection band marked in bold.

background depths with which to explore the dependence of WL distortion on source redshift. With only three bands we cannot reliably define photometric redshifts for a sizable proportion of objects, but instead, by reference to the redshift distributions of the well studied deep field surveys, we may reliably define several galaxy populations of differing mean depths in the CC-space covered by the filters used for each cluster.

Three colour selection has also been applied in a similar context to simulations aimed at forecasting the capabilities of WL tomography (Jain, Connolly & Takada 2007; Medezinski et al. 2010). These simulations convincingly demonstrate that greater efficiency is likely by using limited 3-band imaging for WL tomography, rather than by investing greater imaging time in additional bands to improve photometric redshift precision. For our purposes too we show here that a judicious choice of non-orthogonal boundaries in CC-space allows the definition of several distinct redshift samples of differing mean depth, with relatively little overlap in redshift.

Here we rely on well studied deep field surveys to estimate the redshift distribution of these different background populations, using the wide-field COSMOS 30-band photometric redshift survey (Ilbert et al. 2009) and also the deeper GOODS-MUSIC survey which has wide multi-wavelength coverage in 14 bands (from the U band to the Spitzer 8 μ m band) (Grazian et al. 2006).

In § 2 we present the cluster observations and data reduction and in § 3 we explain the selection of background galaxy samples and in § 4 we describe the WL analysis and outline the formalism. In § 5 we derive the WL amplitude and mean redshift information of the background samples, presenting our results regarding the lensing distance-redshift relation. We discuss the requirements for constraining the cosmological model with this method in 6. We summarize and conclude in § 7.

2 SUBARU DATA REDUCTION

We analyze deep images of three intermediate-redshift clusters, A370 ZwCl0024+17 and RXJ1347-11, observed with the wide-field camera Suprime-Cam (Miyazaki et al. 2002) in several optical bands, at the prime focus of the 8.3m Subaru telescope. The clusters are publicly available from the Subaru archive, SMOKA⁵. Subaru reduction software (SDFRED) developed by Yagi et al. (2002) is used for flat-fielding, instrumental distortion correction, differential re-

¹ <http://www.lsst.org/lsst>

² <https://www.darkenergysurvey.org/>

³ <http://jdem.gsfc.nasa.gov>

⁴ <http://sci.esa.int/science-e/www/object/index.cfm?objectid=42266>

⁵ <http://smoka.nao.ac.jp>

fraction, sky subtraction and stacking. Photometric catalogs are created using SExtractor (Bertin & Arnouts 1996). Since our work relies much on the colours of galaxies, we prefer using isophotal magnitudes. We use the COLORPRO (Coe et al. 2006) program to detect in the R_C -band and measure colours through matched isophotes in the other two bands. Astrometric correction is done with SCAMP (Bertin 2006) using reference objects in the NOMAD catalogue (Zacharias et al. 2004) and the SDSS-DR6 (Adelman-McCarthy et al. 2008) where available. The observational details are listed in Table 1.

3 SAMPLE SELECTION FROM THE COLOUR-COLOUR DIAGRAM

For each cluster we use Subaru observations in three broad optical passbands and all observations are of good seeing, representing some of the highest quality imaging by Subaru in terms of depth, resolution, and colour coverage. We first describe how we separate the background galaxies from foreground and cluster galaxies, combining WL measurements and the distribution of objects in the CC plane and their clustering relative to the center of the cluster. We then examine the redshift distribution of objects selected to lie in the background using the CC plane with reference to the COSMOS field where deep photometric redshifts are established to faint limits using 30 independent passbands covering a very wide range of wavelength.

Note that with only three bands, only a small fraction of the objects have well defined photometric redshifts, in the sense of having a single, narrow peak in their probability $p(z)$, and therefore their use to separate among different redshift populations is very limited. Using the BRz' CC space in this way with reference to the now well established redshift surveys is arguably more reliable in separating galaxy populations of differing depths, in agreement with the simulations of Jain et al. (2007).

In our previous analysis of these data, Medezinski et al. (2010, hereafter M10), we demonstrated how the cluster and foreground galaxies can be reliably identified and separated from background galaxies in the CC diagram, using B_J, R_C, z' bands (Fig. 1). We found in the field of A370 the prominent overdensity of galaxies centered on $B_J - R_C \sim 2$ and $R_C - z' \sim 0.8$ denotes the red-sequence of cluster galaxies (see Fig. 1, left-hand panel, where this overdensity is enclosed by dashed white line). This was also shown by the relatively small mean distance from cluster center of galaxies in that region in CC space (Fig. 1 in M10). The WL measurements for this population of objects is very close to zero, with a measured tangential distortion profile, $g_T(r)$, consistent with zero all the way out to the virial radius, as expected for cluster galaxies which are unlensed. The main central overdensity around $B_J - R_C \sim 1$ and $R_C - z' \sim 0.3$ consists of many foreground galaxies (see Fig. 1, left-hand panel, with an overdensity enclosed by solid white line). These galaxies show a very low level g_T compared to the reference background, marked in gray on Fig. 1 (right panel), and their surface density profile shows only modest central clustering (see M10) indicating that most of these objects lie in the foreground of the cluster. When selecting background galaxies we stay well away from these regions of CC

space which are dominated by cluster and foreground galaxies to minimize contamination by these unlensed galaxies, as described below.

To identify background populations in M10, we took into account both the WL signal and the density distribution of galaxies in the CC plane. In CC space a relatively red population can be rather well defined, dominated by an obvious overdensity (around $B_J - R_C \sim 0.5$ and $R_C - z' \sim 0.8$), and the bluest population is confined to a separate cloud (around $B_J - R_C \sim 0.3$ and $R_C - z' \sim 0.2$) of faint galaxies with a clear lensing signal. Looking at the WL profiles of the red and blue samples, we see very similar behaviour, with a continuous rising signal toward the cluster center. Both cases show good agreement with each other (M10). Combined together, they form our **reference background** sample, to which all the other samples we derive below will be normalized.

The validity of our selection was also demonstrated in M10 by comparison with the spectral evolution of galaxies calculated with the stellar synthesis code Galev⁶ (Kottulla et al. 2009). Here we overlay the CC diagram with colour-tracks of galaxy models: E-type (exponentially declining SFR with Z_\odot), S0 (gas-related SFR with Z_\odot), Sa (gas-related SFR with $2.5Z_\odot$), and Sd (constant SFR with $0.2Z_\odot$). These evolutionary tracks originate in the low-redshift cloud we established as foreground in CC space and evolve to higher redshift passing through the cluster redshift and then to bluer colours as shown in Fig. 5 (right), and finally end at the top-left corner of our CC space, dropping out of the B_J -band at a redshift of $z \sim 3.5$.

In this paper we add additional samples of background galaxies. Two samples will consist of galaxies at redshifts not far beyond that of the cluster, which we term “orange” and “green”. These are selected to lie on the upper-right of the CC space, corresponding reasonably to colour-tracks of E/S0 galaxies which are predicted to show a bend in the CC plane, becoming bluer ($B_J - R_C \sim 2 - 2.5$ and $R_C - z' \sim 1 - 1.5$) toward higher redshift, matching well our observed distribution. A third group comprises the red-cloud described above, centered on $B_J - R_C \sim 0.5$ and $R_C - z' \sim 0.8$, we call the “red” sample. This sample consists of an overdensity of background galaxies from the known “red” branch of the bimodality of field galaxies colours (Capak et al. 2007). A fourth sample consists of the prominent blue peak identified as background galaxies, lying at redshifts beyond the red galaxies, corresponding to the “blue” branch of the colour bimodality, where the colour-tracks turn redder at $B_J - R_C$ as the UV-flux starts to drop out of the blue B_J band with increasing redshift, above a redshift of approximately, $z \sim 2$. Finally, we select galaxies from the top-left corner of the CC plane, corresponding to the predicted location of B_J -dropout galaxies at an average redshift of $z \sim 3.5$.

For each sample selected we examine the colour boundaries of each sample as a function of the WL signal, to ensure we keep well clear of foreground or cluster members which otherwise dilute the WL signal of background galaxies. This approach has been investigated in our earlier work, where this problem was first identified as a major problem for WL work and rectified using appropriate CC-selection (Medezin-

⁶ <http://www.galev.org/>

ski et al. 2007; Umetsu & Broadhurst 2008; Medezinski et al. 2010; Umetsu et al. 2010).

We apply this selection scheme for two more clusters, ZwCl0024+17 and RXJ1347-11, though here the data is not as deep. Furthermore, the colour coverage is less wide in the case of RXJ1347-11 (only $V R z'$) allowing the selection of the corresponding orange, green, red and blue background samples, as above, but not sufficient for separation of dropout galaxies for a significant WL detection.

The greater depth of the A370 imaging allows us to further divide the green, red and blue background samples into independent bright and faint subsamples for our WL measurements. For each of these samples, we now estimate their average WL signal, by comparing the tangential distortion measurements to that of the reference background sample, and derive what we call mean “ g_T amplitude” (see § 5.1). Subsequently, we also estimate the median redshift from the COSMOS photo- z catalogue and its equivalent d_{ls}/d_s (see § 5.2). We summarize the properties of the selected samples in Table 2.

4 WEAK LENSING MEASUREMENTS

To make the WL catalogs, we use the IMCAT package developed by N. Kaiser⁷ to perform object detection and shape measurements, following the formalism outlined in Kaiser, Squires & Broadhurst (1995, hereafter KSB). Our analysis pipeline is described in Umetsu et al. (2010). We have tested our shape measurement and object selection pipeline using STEP (Heymans et al. 2006) data of mock ground-based observations (see Umetsu et al. 2010, § 3.2). Full details of the methods are presented in Umetsu & Broadhurst (2008), Umetsu et al. (2009) and Umetsu et al. (2010).

The shape distortion of an object is described by the complex reduced-shear, $g = g_1 + ig_2$, where the reduced-shear is defined as:

$$g_\alpha \equiv \gamma_\alpha / (1 - \kappa). \quad (1)$$

The tangential component g_T is used to obtain the azimuthally averaged distortion due to lensing, and computed from the distortion coefficients g_1, g_2 :

$$g_T = -(g_1 \cos 2\theta + g_2 \sin 2\theta), \quad (2)$$

where θ is the position angle of an object with respect to the cluster centre, and the uncertainty in the g_T measurement is $\sigma_T = \sigma_g / \sqrt{2} \equiv \sigma$ in terms of the RMS error σ_g for the complex shear measurement. To improve the statistical significance of the distortion measurement, we calculate the weighted average of g_T and its weighted error, as

$$\langle g_T(\theta_n) \rangle = \frac{\sum_i u_{g,i} g_{T,i}}{\sum_i u_{g,i}}, \quad (3)$$

$$\sigma_T(\theta_n) = \sqrt{\frac{\sum_i u_{g,i}^2 \sigma_i^2}{(\sum_i u_{g,i})^2}}, \quad (4)$$

where the index i runs over all of the objects located within the n -th annulus with a median radius of θ_n , and $u_{g,i}$ is the inverse variance weight for i -th object, $u_{g,i} = 1/(\sigma_{g,i}^2 + \alpha^2)$,

where α^2 is the softening constant variance. We choose $\alpha = 0.4$, which is a typical value of the mean RMS $\bar{\sigma}_g$ over the background sample. We accurately combine the photometry with weak-lensing measurements of as many galaxies as possible, discarding objects below the seeing limit (given in table 1) plus two standard deviation of that value in the detection band, to remove stars and avoid unreliable shape measurements.

4.1 Formalism: Relative Distortion Strength

For a given source redshift z_s and a fixed lens redshift z_l , the observable (complex) reduced gravitational shear $g(z_s)$ in the subcritical regime is expressed in terms of the gravitational shear γ and the lens convergence κ as (e.g., Seitz & Schneider 1997; Medezinski et al. 2007)

$$g(z_s) = \gamma(z_s)(1 - \kappa[z_s])^{-1} = \gamma_\infty \sum_{k=0}^{\infty} \beta^{k+1}(z_s) \kappa_\infty^k \quad (5)$$

where κ_∞ and γ_∞ are the lensing convergence and the gravitational shear, respectively, calculated for a hypothetical source at $z_s \rightarrow \infty$, and $\beta(z_s)$ is the lensing strength of a source at z_s relative to a source at $z_s \rightarrow \infty$, $\beta(z_s) \equiv D(z_s)/D(z_s \rightarrow \infty)$; $D(z_s) \equiv d_{ls}/d_s$. Hence, the reduced shear averaged over the source redshift distribution is expressed as

$$\langle g \rangle = \gamma_\infty \sum_{k=0}^{\infty} \langle \beta^{k+1} \rangle \kappa_\infty^k, \quad (6)$$

where $\langle \beta^k \rangle$ is defined such that

$$\langle \beta^k \rangle \equiv \frac{\int dz_s N(z_s) \beta^k(z_s)}{\int dz_s N(z_s)} \quad (7)$$

with the redshift distribution $N(z_s)$. In the WL limit where $|\kappa_\infty|, |\gamma|_\infty \ll 1$, then

$$\langle g \rangle \approx \langle \beta \rangle \gamma_\infty = \langle \gamma \rangle. \quad (8)$$

Thus, the mean reduced shear is simply proportional to the mean lensing strength, $\langle \beta \rangle \propto \langle D \rangle$. The next order approximation is

$$\langle g \rangle \approx \langle \gamma \rangle (1 + f_\beta \langle \kappa \rangle) \approx \frac{\langle \gamma \rangle}{1 - f_\beta \langle \kappa \rangle}, \quad (9)$$

where $f_\beta \equiv \langle \beta^2 \rangle / \langle \beta \rangle^2$ is a redshift-moment ratio of the order of unity (Seitz & Schneider 1997).

Since the tangential distortion signal, g_T , is a function of cluster radius, we first decompose the tangential distortion profile of our background sample (B), defined above as our reference (see § 3), into the following form:

$$g_{T,B}(\theta) = a_B \theta^{-b_B}, \quad (10)$$

where the radial shape of $g_T(\theta)$ is assumed to be a single power-law with a power index b_B , and a_B represents the distortion amplitude of our reference background. In practice, we fit the outer profile of $g_T(\theta)$, excluding the nonlinear regime ($\theta \lesssim 1$), to the power-law model, constraining simultaneously the distortion amplitude a_B and the outer slope, b_B . Next, for each of our other defined samples, we fit a power law with the same slope b_B , but allow the amplitude a_i to vary:

⁷ <http://www.ifa.hawaii.edu/~kaiser/imcat>

Table 2. CC-selected Sample Properties

Cluster	Sample	magnitude limits	N	\bar{n} arcmin ⁻²	Γ (g_T -amplitude ratio)	χ^2/dof (PL)	$\langle z_s \rangle$
A370	foreground	$18 < z' < 22$	1235	1.3	-0.04	13/6	0.33
	orange	$19 < z' < 23$	450	0.5	0.41	1/6	0.73
	green-bright	$20 < z' < 22.5$	839	0.9	0.85	11/6	0.9
	green-faint	$22.5 < z' < 25$	1240	1.3	0.88	6/7	0.99
	red-bright	$22 < z' < 24$	5454	5.6	0.87	17/8	1.11
	red-faint	$24 < z' < 26$	6986	7.1	1.1	27/8	1.14
	blue-bright	$23 < z' < 24.6$	1679	1.7	0.95	6/8	1.79
	blue-faint	$24.6 < z' < 25.5$	2857	2.9	1.15	23/8	1.78
	drops	$24 < z' < 26.5$	1529	1.6	1.3	13/8	3.86
	background	$22 < z' < 26$	19362	19.8	1	19/8	1.31
ZwCl0024+17	foreground	$18 < z' < 22$	734	0.9	0.08	5/9	0.29
	orange	$18 < z' < 23$	687	0.9	0.55	11/9	0.73
	green	$21 < z' < 25$	1582	2	0.83	23/9	0.98
	red	$21 < z' < 25.5$	7716	9.7	0.97	8/9	1.11
	blue	$23 < z' < 25$	2420	3	0.99	13/9	1.62
	drops	$25 < z' < 27$	625	0.6	0.93	23/9	3.71
	background	$21 < z' < 25.5$	10488	13.1	1	7/8	1.24
RXJ1347-11	foreground	$19 < z' < 24$	2452	3.4	-0.04	14/8	0.43
	orange	$19 < z' < 26$	473	0.5	0.76	5/8	0.76
	green	$21 < z' < 25$	1296	1.1	1.1	5/8	0.94
	red	$21 < z' < 26$	4880	3.9	0.92	9/8	1.11
	blue	$23.5 < z' < 26$	1509	2.1	1.18	35/8	1.95
	background	$21 < z' < 26$	7139	6.3	1	4/6	1.24

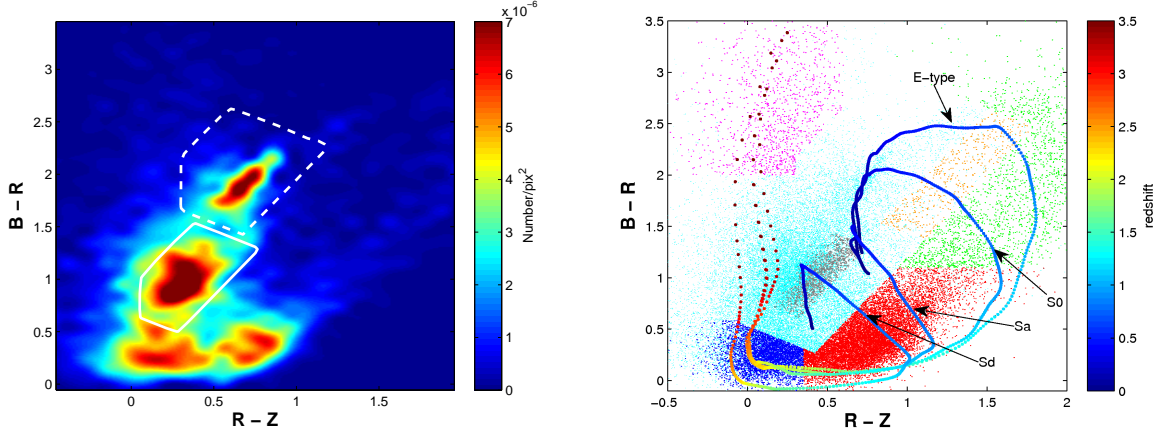


Figure 1. *Left:* Number density in $B_J - R_C$ vs. $R_C - z'$ CC space for A370. The four distinct density peaks are shown to be different galaxy populations - the reddest peak in the upper right corner of the plots (dashed white line) depicts the overdensity of cluster galaxies, whose colours lay on the red sequence; the middle peak lying blueward of the cluster comprises mainly foreground galaxies (solid white line); the two peaks in the bottom part (bluest in $B_J - R_C$) can be demonstrated to comprise of blue and red background galaxies. Together, the red+blue galaxies will serve as our “reference” background sample for WL purposes. *Right:* $B_J - R_C$ vs. $R_C - z'$ CC diagram, showing the distribution of galaxies in A370. Marked are the selected foreground sample (gray) and background samples: orange (orange), green (green), red (red), blue (blue) and dropout (magenta) background galaxies, selected to include galaxies lying away from the cluster and foreground regions. Overlaid are synthetic colour tracks including evolution, calculated with the Galev code for an elliptical, S0, Sa and Sd type models.

$$g_{T,i}(\theta) = a_i \theta^{-b_B}. \quad (11)$$

Therefore, if we calculate the lensing signal of i -th sample relative to the reference background (B),

$$\Gamma_i \equiv g_{T,i}(\theta)/g_{T,B}(\theta) = a_i/a_B. \quad (12)$$

From equation (8), we obtain the following expression in the WL approximation ($|\langle \kappa \rangle|, |\langle \gamma \rangle| \ll 1$):

$$\Gamma_i = a_i/a_B \approx \langle \beta \rangle_i / \langle \beta \rangle_B = \langle D \rangle_i / \langle D \rangle_B, \quad (13)$$

where $\langle \rangle_i$ ($i = 1, 2, \dots, B$) represents averaging over the redshift distribution $N_i(z_s)$ of i -th galaxy sample. The relative distortion strength Γ_i can be regarded as a function of the discrete background sample i with the redshift distribution $N_i(z_s)$, which is observationally available and calibrated by deep, multi-band blank surveys such as the COSMOS survey. For a given cosmological model, one can readily construct its theoretical prediction Γ_i ($i = 1, 2, \dots, B$) using a set of redshift distribution functions $N_i(z_s)$. The function Γ_i can be formally labeled by its mean redshift

$$\langle z_s \rangle_i \equiv \int dz_s N_i(z_s) z_s / \int dz_s N_i(z_s) \quad (14)$$

which is independent of the cosmological model.

To the next order of approximation, the distortion amplitude ratio is written as (Appendix B of Medezinski et al. 2007)

$$\Gamma_i = \frac{\langle D \rangle_i}{\langle D \rangle_B} \{1 + (f_{\beta,i} \langle \beta \rangle_i - f_{\beta,B} \langle \beta \rangle_B) \kappa_\infty(\theta) + O(\kappa_\infty^2)\} \quad (15)$$

with $f_{\beta,i} \equiv \langle \beta^2 \rangle_i / \langle \beta \rangle_i^2$ and $f_{\beta,B} \equiv \langle \beta^2 \rangle_B / \langle \beta \rangle_B^2$. The next order correction term is proportional to $(f_{\beta,i} \langle \beta \rangle_i - f_{\beta,B} \langle \beta \rangle_B) \kappa_\infty(\theta)$, which is much smaller than unity for the galaxy samples of our interest in the mildly nonlinear regime ($\theta \gtrsim 1$). We thus simply adopt equation (13) obtained in the WL approximation. This can be further justified by the fact that the slope parameter b_B is constrained by a least χ^2 fit to the outer distortion profile. The mean weighted cluster radius $\langle \theta \rangle \equiv \sum_i u_{g,i} \theta_i / \sum_i u_{g,i}$ used for a fit is $\langle \theta \rangle \sim 10-11$ arcmin for our clusters, where the weak lensing approximation is valid.

5 RESULTS

5.1 Weak lensing profiles

For each cluster, a reference background sample has been defined (explained above in § 3). The WL tangential distortion, g_T , vs. distance from cluster center, θ , of each reference background is plotted in Fig. 2 (black crosses). Each reference background sample is fitted by a power-law according to Eq. 10, but only in the WL regime, i.e., outside $\theta \gtrsim 1'$. The fit is estimated using two ways – we fit the entire sample dataset, weighting each galaxy $g_{T,i}$ by $u_{g,i}$ (see § 4), and we also fit the binned g_T profile, $\langle g_T(\theta_n) \rangle$, weighting by the bin error, $1/\sigma_{T^2}(\theta_n)$. We find good consistency between the two fitting schemes. The goodness-of-fit χ^2 values of the binned fit are displayed next to each power-law fit, and also in Table 2. As can be seen, a simple power-law serves as a reasonable fit in all cases.

For each of our defined samples (foreground, orange, green, red, blue and dropouts) we again plot g_T vs. radius in Figure 4 (gray, orange, green, red, blue and dropouts, respectively, top to bottom panels of each cluster). We fit each sample with the same power-law index, b_B , given by its relevant reference background (the sample fit is shown as dashed black line with $1 - \sigma$ confidence bounds, and the reference background fit is also shown as a dotted line). The WL amplitude of each sample relative to the reference background is given in each panel as $\Gamma_i \equiv a_i/a_B$ (as defined by Eq. 12) and detailed in Table 2. We see that indeed, for

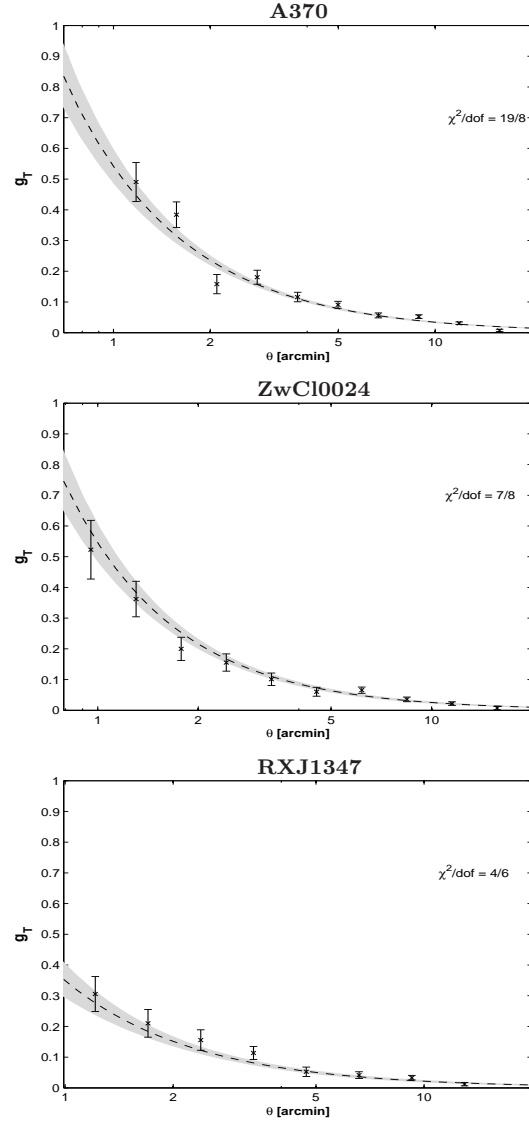


Figure 2. Tangential distortion g_T vs. distance from cluster center for A370 (top), ZwCl0024+17 (middle) and RXJ1347-11 (bottom) reference background samples. Overlaid is the power-law fit (dashed black line) with $1 - \sigma$ confidence levels (shaded region) and the PL-fit χ^2 is indicated.

the foreground samples, the $g_T(\theta)$ profile agrees with zero throughout, and gives a relative WL amplitude of zero.

As another consistency check, we plot the galaxy surface number density vs. radius for A370 samples in Figure 3. As can be seen, no clustering is observed toward the center for any of the samples, which demonstrate that there is no contamination by cluster members in the samples comprising only background members. The foreground sample (gray triangles) shows a modest increase in number density (factor of 2 increase from $\theta = 20$ to $\theta = 2$) compared to the cluster, despite the exclusion of the cluster early-type galaxies by colour. Bluer later-type cluster members are to be expected here given the redshift window sampled by reference to Figure 6, which shows that the tail of the distribution reaches just beyond the redshift of A370 § 5.2).

The data for A370 represents the best available data,

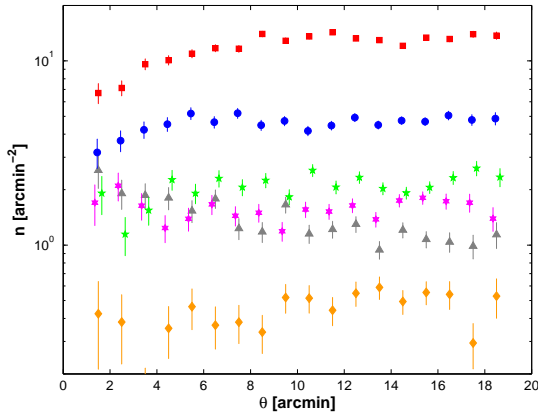


Figure 3. Galaxy surface number density vs. radius for A370 foreground sample (gray triangles), orange (orange diamonds), green (green pentagrams), red (red squares), blue (blue circles) and dropout (magenta hexagrams) background samples.

both in terms of the filter coverage – B, R, z' , and in terms of total exposure times in each band. For RXJ1347-11 we only have V, R, z' coverage, making it somewhat harder to set apart the different populations, and also dropping out between V and R is not as clear since the two filters are less well separated in wavelength, preventing us from selecting a dropout sample. For ZwCl0024+17 we do have B, R, z' , but the z' band is much shallower.

5.2 COSMOS photometric redshifts

To estimate the respective depths of the different samples defined above from our Subaru photometry, we make use of the accurate photometric redshifts derived for the well studied multi-band field survey, COSMOS (Capak et al. 2007). For COSMOS, photometric redshifts have been derived by Ilbert et al. (2009) using 30 bands in the UV to mid-IR. Since the COSMOS photometry does not cover the Subaru R_C band, we estimate R_C -band magnitudes for it. For this we use the HyperZ (Bolzonella, Miralles & Pelló 2000) template fitting code to obtain the best-fitting spectral template for each galaxy, from which the R_C magnitude is derived with the transmission curve of the Subaru R_C -band filter (see Umetsu et al. 2010).

We then select samples by applying the same CC/magnitude limits as we did above for each of our clusters – A370, ZwCl0024+17 and RXJ1347-11. This is shown in Fig. 5 (left) for the COSMOS catalogue and plotted in terms of the same CC plane as A370. The colour distribution of COSMOS field galaxies seen in this B, R, z' CC-space is very similar to that of A370, displaying the same morphology, including red, blue and dropout populations, but without the density peak associated with the massive cluster A370. We also show how redshift varies in this CC-plane by calculating the mean photo- z redshift from COSMOS in fine bins over the CC plane (Fig. 5, right), with the samples boundaries displayed as well. This demonstrates that the main overdensity in the CC plane near $B_J - R_C \sim 1$ and $R_C - z' \sim 0.3$ has a mean redshift of around $z \lesssim 0.5$, which agrees with our estimation for A370 where we found very lit-

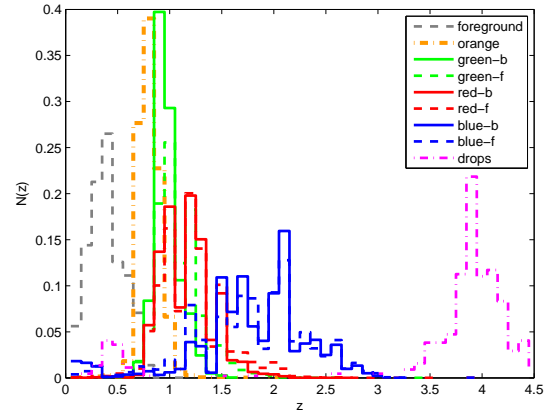


Figure 6. Redshift distribution of all A370 samples: foreground (dashed gray), orange (dotted-dashed orange), green (green) bright (solid) and faint (dashed), red (red) bright (solid) and faint (dashed), blue (blue) bright (solid) and faint (dashed), and dropout (dotted-dashed magenta) using COSMOS photo- z 's.

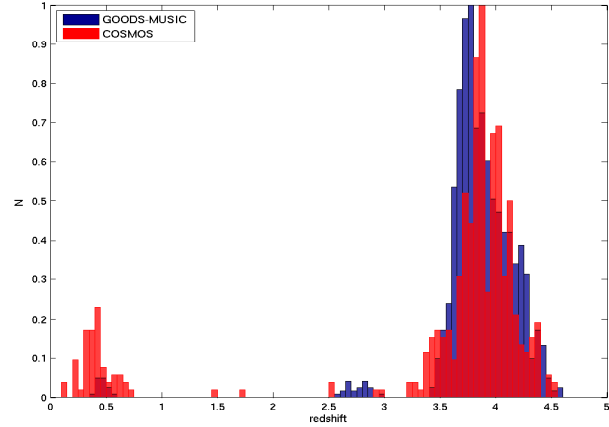


Figure 7. Redshift distribution of the dropout-selected sample using COSMOS photo- z 's (light red) and using GOODS-MUSIC photo- z 's (dark blue). The low- z peak seen more notably from the COSMOS photo- z 's is most likely due to misclassified galaxy redshifts, supported by the smaller numbers found when using the GOODS-MUSIC photo- z catalogue.

tle WL signal implying these object lie predominantly in the foreground of the cluster. We also see from this figure that the region where we picked “red” galaxies corresponds to $z \sim 1 - 1.5$, and the “blue” galaxies occupy a region of mean redshift around $z \sim 2$. Most notably, the top left corner of “dropout” galaxies corresponds to high- z with $z \gtrsim 3.5$. We further plot the redshift distribution of all the samples in Fig. 6. We calculate the median redshift of each sample and summarized in Table 2.

However, if we look at the distribution of COSMOS redshifts of the dropout sample (Fig. 7, red), we find it is somewhat double-peaked, with most galaxies lying around $z \sim 3.5$, but a significant fraction identified as having $z \sim 0.4$. Since we are certain most of the galaxies in this region are in fact high redshift dropout galaxies, justified by the apparent high WL distortions measured for these

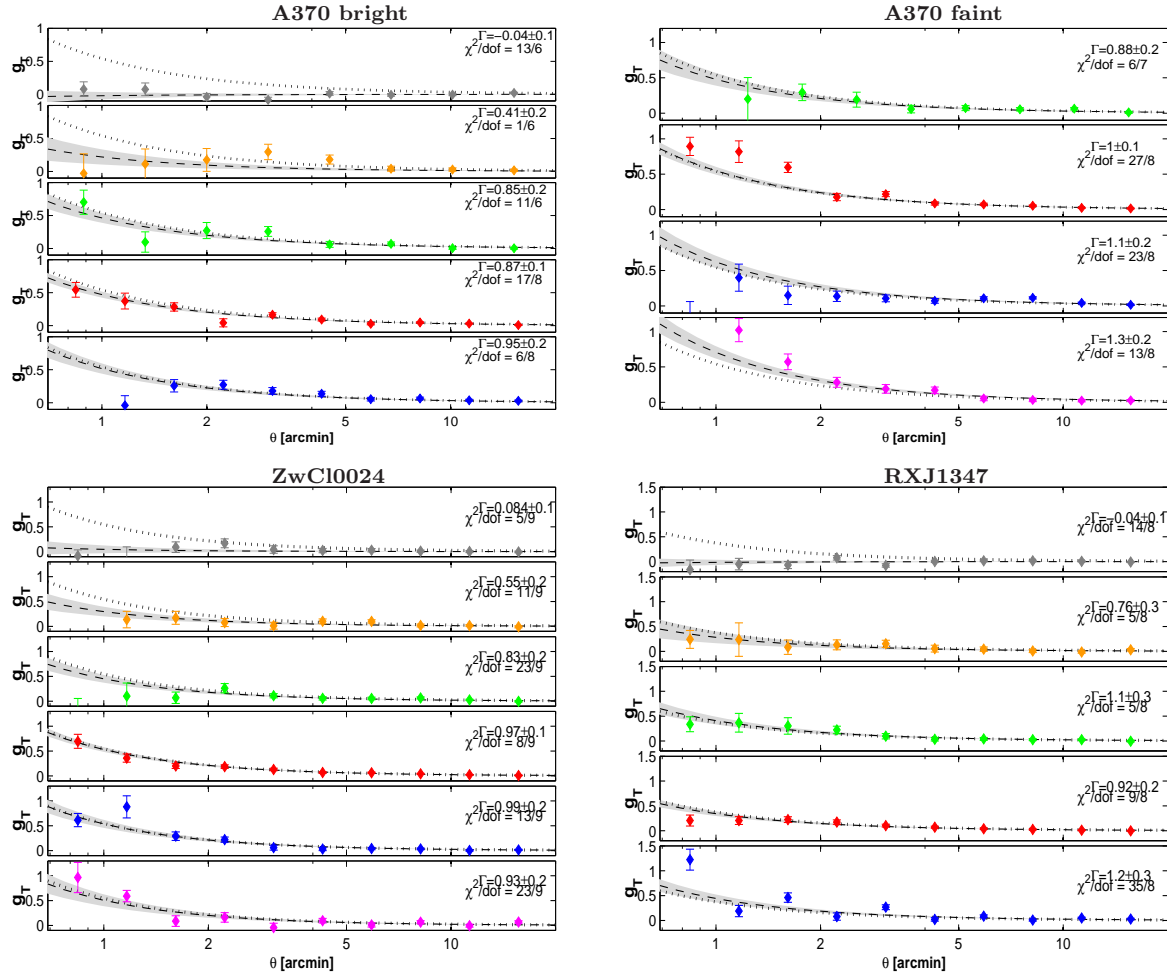


Figure 4. g_T vs. cluster radius for A370 bright samples (top left: foreground, orange, green, red & blue) and faint (top right: green, red, blue & dropouts), ZwC10024+17 (bottom left: foreground, orange, green, red, blue & dropouts) and RXJ1347-11 (bottom right: foreground, orange, green, red & blue), where the fixed power-law fit is overlaid (dashed black line) with $1 - \sigma$ confidence levels (shaded region). Also plotted is the power-law fit of the equivalent “reference” background sample (dotted curve). In each case the resulting normalized g_T amplitude ratio, Γ , is denoted next to the profile.

galaxies (see Fig. 4) and by reference to deep spectroscopic work in this rising plume of “dropout” galaxies (Steidel et al. 1999), we may conclude the low redshifts assigned to some of these galaxies may be misclassified as low redshift early type/dusty galaxies in the photo- z catalogue of the COSMOS field. This is not surprising, since at faint magnitudes the COSMOS photo- z have a relative high catastrophic failure rate (Ilbert et al. 2009).

We further examine this issue using the somewhat deeper GOODS-MUSIC catalogue (Grazian et al. 2006; Santini et al. 2009), which has 15 bands, including high quality ACS photometry (GOODS-S) and deep IRAC imaging which is very helpful in reducing the outlier rate a high- z . Using the z' -band selected GOODS-MUSIC photo- z , we derive a spectral classification for each galaxy using a library of ~ 200 PEGASE (Fioc & Rocca-Volmerange 1997) templates very similar to that described in Grazian et al. (2006), as included in the EAZY software (Brammer et al. 2009), and then calculate Subaru magnitudes for all the galaxies using the BPZ (Benítez 2000) code.

By making the same CC selection, we plot the redshift

distribution of the same dropout sample (Fig. 7, blue), but here practically no low- z peak is observed, and all galaxies in this region are estimated to have high redshifts, $z \gtrsim 2.5$. This comparison between COSMOS and GOODS-MUSIC redshifts allows us to securely set a conservative lower $B - R$ limit to avoid inclusion of real low- z objects. We can thus safely assume all objects identified as low- z in the COSMOS catalogue are largely mistakenly classified, a point also made in relation to this by Schrabback et al. (2010). Estimating the median redshift of the dropout sample gives $z \simeq 3.8$, a value very close to the mean redshift of all galaxies lying above $z > 1.5$ galaxies. This further demonstrates the low- z peak is a low-significance contamination. A further examination of the photometric redshift estimation for such objects in the COSMOS field seems worthwhile in view of these results.

5.3 Lensing strength dependence on magnitude

As another check, we plot Γ , the g_T -amplitude ratio, vs. z' -band magnitude for A370 selected samples, to see if there is

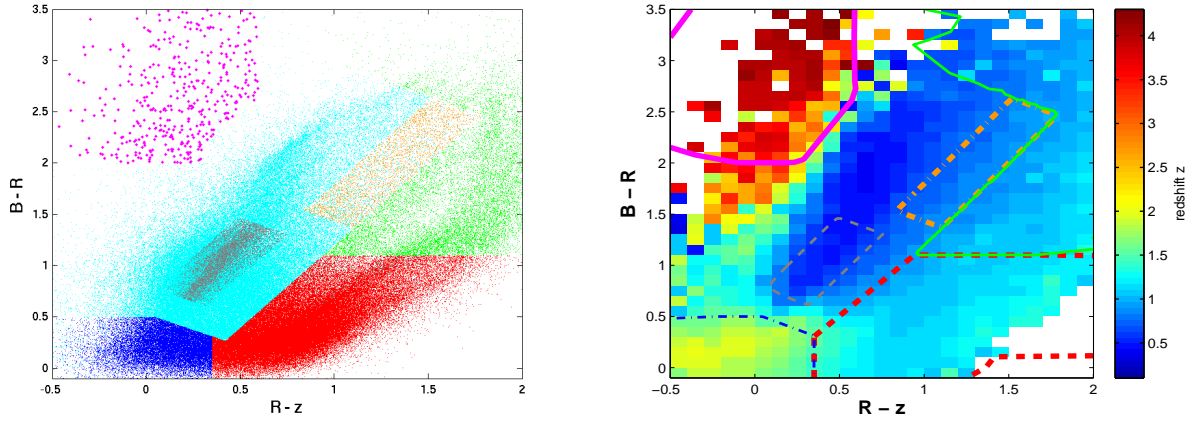


Figure 5. *Left:* $B_J - R_C$ vs. $R_C - z'$ CC diagram, showing the distribution of galaxies in COSMOS field. Applying the same CC-cuts as our selection for A370, we define galaxy samples: foreground (gray), orange (orange), green (green), red (red), blue (blue), and dropout (magenta) galaxies, in order to estimate the mean redshifts and mean depths of these samples using COSMOS photo- z 's. *Right:* Average COSMOS redshift in CC bins. Overlaid are the boundaries of the foreground (thin dashed gray line), orange (thick dotted-dashed orange line), green (thin solid green line), red (thick dashed red line), blue (thin dotted-dashed blue line) and dropout (thick solid magenta line) samples selected in the COSMOS field according to A370 CC-cuts. Evidently, different regions of CC space correspond to different redshift populations of galaxies. Most notably, The top left corner denotes dropout galaxies of $z \gtrsim 3.5$, corresponding well to our selection of highly distorted dropout galaxies.

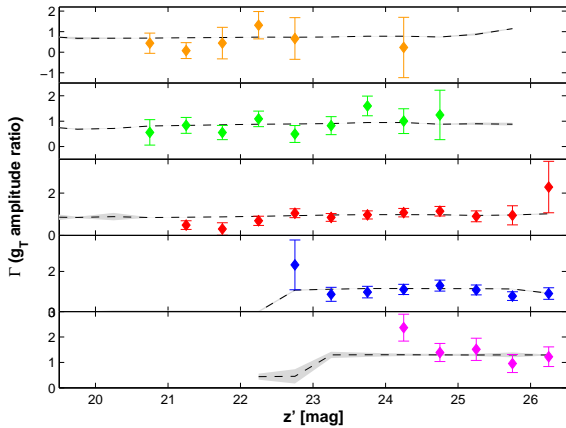


Figure 8. Γ , the g_T amplitude ratio, vs. magnitude (z' band) for A370 orange, green, red, blue and dropout galaxy samples (top to bottom). Overlaid is the lensing depth, d_{ls}/d_s , vs. magnitude calculated from COSMOS photo- z 's for each of the samples (dashed black line) with $1 - \sigma$ confidence levels (shaded region).

any trend of the lensing amplitude with magnitude. We also plot the mean d_{ls}/d_s as a function of magnitude (all values normalized to the reference background values) calculated in independent magnitude bins for each sample using the COSMOS photo- z catalogue. This serves as a further consistency check. Interestingly, for the blue galaxies (and the dropout galaxies to some extent), the mean signal seems to drop slightly with fainter magnitudes. This trend is somewhat counter-intuitive, since we expect that fainter galaxies will be at higher redshifts, and therefore have on average a higher signal.

The diminished WL signal could possibly hint at a problem with estimating the WL signal from faint **blue** galaxies, which are in general quite irregular in morphology, and em-

pirical simulations with higher space based resolution can be made to examine this better. The declining trend of the predicted d_{ls}/d_s in the case of blue galaxies, based on the COSMOS photo- z estimation, shown in Fig. 8 (dashed curves), could possibly point to a miss-classification of blue galaxies with photo- z methods, a well known problem for blue galaxies, or even simply a limiting magnitude beyond which the photo- z method fails in this catalogue. We set our magnitude limits conservatively to minimize these possible problems, with $19 < z' < 23$ for the orange sample, $20 < z' < 24.5$ for the green sample, $23 < z' < 25$ for the blue sample, $22 < z' < 26$ for the red sample, and $24.5 < z' < 26.5$ for the dropout sample, in the case of A370. Similar examination and limits were also applied for ZwCl0024+17 and RXJ1347-11, with results discussed below.

5.4 Lensing strength vs. redshift

We may now finally combine the WL distortion information with the redshift information for all the samples of background galaxies defined above. First, we plot the WL amplitude, a , as a function of redshift in Fig.9 for the three clusters – A370 (top), ZwCl0024+17 (middle) and RXJ1347-11 (bottom). A clear trend of increasing WL amplitude is seen with redshift, especially in the case of A370. A null result is easily excluded with low significance – $\chi^2/N = 91/8$ for A370, $\chi^2/N = 34/4$ for ZwCl0024+17 and $\chi^2/N = 42/3$ for RXJ1347-11, for a case of non-increasing horizontal line. In order to compare the resulting trend with the cosmological trend, we plot Γ , the g_T -amplitude ratio, against median redshift, $\langle z_s \rangle$, in Fig. 10 for each of the clusters examined – A370 (top), ZwCl0024+17 (middle) and RXJ1347-11 (bottom). The horizontal bars show the width of the source redshift distribution, given as the 68% range of data about the median redshift. Each point in a figure represents an independent sample, where the first point represents the foreground

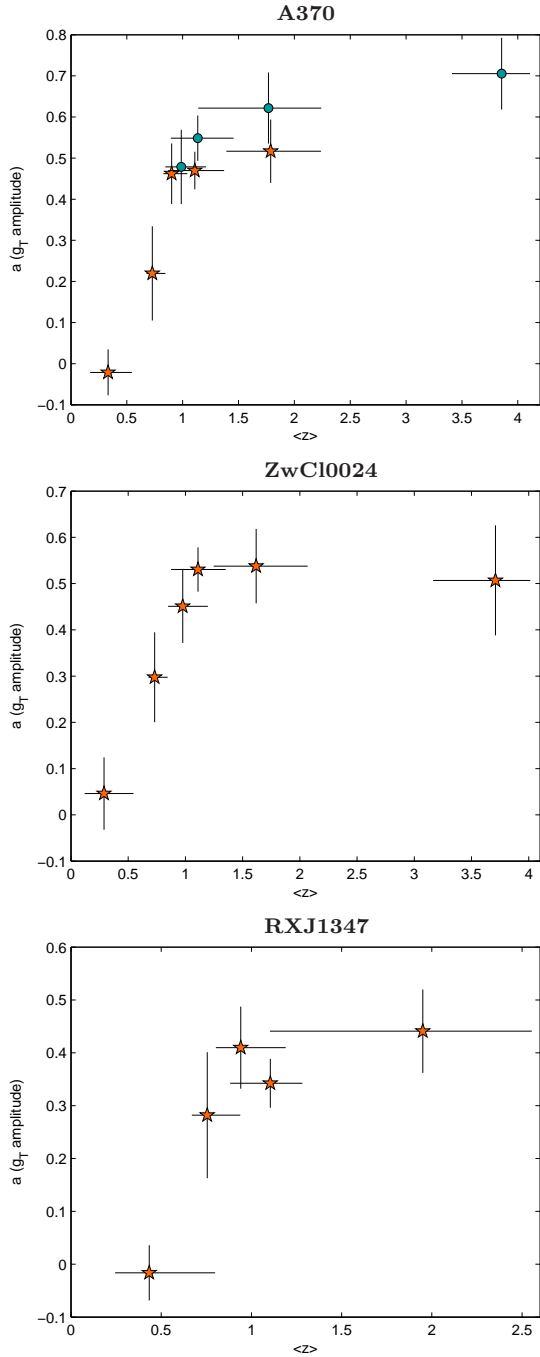


Figure 9. g_T amplitude, a , vs. redshift for A370 (top) bright (stars) and faint (circles) samples, ZwCl0024+17 (middle) and RXJ1347-11 (bottom). A trend of higher WL amplitude with redshift is seen.

sample in front of each cluster, and the other points represent background galaxy samples. For each sample, we also calculate the median lensing distance ratio, $\langle d_{ls}/d_s \rangle$, for each cosmological model – Λ CDM (empty circles), Einstein-de Sitter (crosses), and an empty universe (empty squares), using the COSMOS photo- z measurements of galaxies within the same CC-magnitude boundaries defined for each background sample and thus obtain the predicted depth. We interpolate between these discrete predicted values to pro-

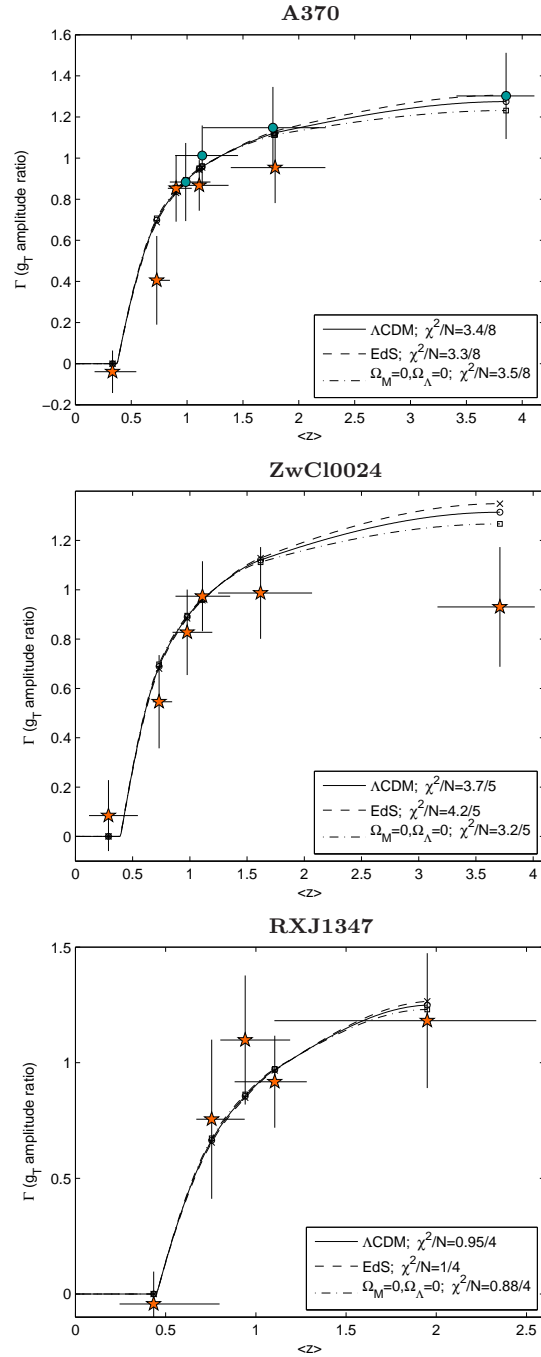


Figure 10. g_T amplitude ratio, Γ , vs. redshift for A370 (top) bright (stars) and faint (circles) samples, ZwCl0024+17 (middle) and RXJ1347-11 (bottom). Also plotted is the lensing depth, d_{ls}/d_s , vs. redshift for different cosmologies – Λ CDM (circles+solid line), Einstein-de Sitter (crosses+dashed line), and an empty Universe (squares+dashed-dotted line) estimated using the COSMOS photometric redshift catalogue. Horizontal bars represent the width of the source redshift distribution, given as the 68% range of data about the median redshift.

vide the theoretical relation, $d_{ls}/d_s(z)$ for each cosmological model. We can thus compare how the WL strength Γ agrees with predicted d_{ls}/d_s . It is quite evident, especially in the case of A370, where we have the best dataset and therefore more data points to compare with, that the WL amplitude agrees well with the theoretical relations for d_{ls}/d_s as a function of redshift. For the other two clusters, ZwCl0024+17 and RXJ1347-11 the data is more shallow and hence noisier as can be seen in Fig. 10 (middle and bottom panels, respectively) but consistency is also found within the errors. Note that in the case of RXJ1347-11 the colour separation is not as good, since the bluest band available is V , rather than B , limiting the separation in depth of the background galaxy populations.

6 CONSTRAINING COSMOLOGICAL PARAMETERS

The clear detection here of the distance-redshift relation from our WL analysis of A370, prompts the question of how many such clusters would be required in order to provide a useful cosmological constraint. This issue has been explored more generally in the context of planned field and cluster surveys by Jain & Taylor (2003); Taylor et al. (2007); Kitching et al. (2007). Taylor et al. (2007) present a detailed analysis of the sensitivity of cosmological cluster surveys to the ratio of shear values measured in independent redshift bins, finding that a large fraction of the potential integrated signal on the sky is contributed by abundant small, cluster mass range ($M \approx 10^{14} M_\odot$), but that a large contribution also comes from the largest clusters, like those studied here.

Here we use an order-of-magnitude calculation to estimate how well our newly approved MCT/CLASH⁸ survey (P.I. M. Postman) can do in this context, for which we aim to complete very high quality WL data for approximately 25 massive clusters, similar in quality to the $B_J R_C z'$ imaging of A370.

As defined above in Eq. (12), Γ , is a shear ratio statistic between any two independent redshift bins summed over N_{cl} clusters, given by:

$$\Gamma_{ij} \approx \frac{\gamma_i}{\gamma_j} = \frac{r[\chi(z_j)]r[\chi(z_i) - \chi(z_l)]}{r[\chi(z_i)]r[\chi(z_j) - \chi(z_l)]}, \quad (16)$$

where $r = r(\chi)$ is the comoving angular diameter distance, $\chi(z)$ is the comoving distance and z_l is the redshift of the lens, and Γ scales with the dark energy equation of state parameter, w , as $\Gamma \approx |w|^{-0.02}$ (Taylor et al. 2007). The fractional error on w is given by (Taylor et al. 2007),

$$\frac{\Delta w}{w} = \frac{2}{\gamma_T} \left(\frac{d \ln \Gamma}{d \ln w} \right)^{-1} \frac{\sigma_e}{\sqrt{N_b}}, \quad (17)$$

where γ_T is the typical mean tangential shear of each cluster, and $\sigma_e = 0.3$ is the measured intrinsic scatter in galaxy ellipticity per mode (KSB), and N_b is the total number of galaxies summed up behind all the clusters co-added for this purpose.

Assuming $\gamma_T \approx 0.05$ and $N_b \approx 0.6 \times 10^6$, summed over the available background for 25 clusters, (taking A370 as

our guide to the number of background galaxies detected per cluster) we find from Eq. (17) the expected precision on w from our sample is $\Delta w/w \approx 0.8$. While this seems a relatively large uncertainty, the first application of the method by Kitching et al. (2007) suggests that the error distribution is non-Gaussian, with a rather sharp cut-off at high values of w placing a relatively tight upper limit. Other geometric probes currently do not succeed much better than this individually, e.g., from Baryon acoustic oscillations and SN-Ia, $\Delta w \approx 0.3$. Furthermore, the shear-ratio test has a different degeneracy with respect to the cosmological parameters to other probes, making even a crude measurement worthwhile.

This constraint may be improved upon by conducting a more careful analysis incorporating a proper likelihood function with reasonable priors for estimating the shear signal and redshift dependence. In addition, the photometry may be optimised for this purpose with emphasis on maximising dropout populations so that a wider redshift coverage may be achieved for better defining the distance-redshift relation.

7 DISCUSSION & CONCLUSIONS

Using deep observational data, the dependence of the amplitude of WL with source distance has been measured for individual massive galaxy clusters using independent samples of foreground and background galaxies of differing depths, with a visible increasing trend. This is most clearly visible for A370 where we have Subaru imaging of relatively high quality in B , R and z' bands, allowing us to further subdivide these samples into independent bright and faint populations. A general increasing trend with redshift is also seen for the other two clusters, albeit noisier than for A370. These clusters datasets are less deep, and with a reduced colour coverage (only V, R, z' in the case of RXJ1347-11), demonstrating the advantage of depth and the wide bandwidth coverage of A370. Small number statistics and possible dilution, especially in the case of the dropout samples, may lead to large uncertainties and underestimated values. Our photometry comprises only three optical bands per cluster and so we do not rely on photo- z estimates, but instead we determine the depth of these background populations with reference to the very well studied COSMOS and GOODS-MUSIC fields, by applying CC and magnitude cuts equal to that of our background populations.

For A370, the trend of increasing WL-amplitude with redshift uncovered here follows the expected form of the lensing distance-redshift relation but with uncertainties presently too large to distinguish between cosmologies. The encouraging results from the clusters examined here, most notably for A370, merit further application of this approach to a larger sample of clusters.

The recently approved MCT/CLASH program will observe 25 clusters with *HST* ACS/WFC3, most of which have deep multi-colour Subaru imaging, so that we estimate a WL based precision on w of $\Delta w \approx 0.6$, but with a different degeneracy relative to other probes, complementing existing methods. Combining this WL estimate with the distance-redshift relation from strong lensing will provide an enhanced geometric-based cosmological constraint.

To extract the cosmological parameters from such accurate data will require further refinement of the method. We

⁸ <http://www.stsci.edu/~postman/CLASH/>

must take account of the greater mean depth that lensing magnification generates whose effect on cluster lensing has been explored in some detail previously (Broadhurst et al. 1995), and also a second order correction for the surface density described in § 4.1. These effects, although small in terms of the lensing amplitude, are comparable with the relatively small differences of interest between competing cosmologies and thus must be explored in any serious study of cosmology with this method.

ACKNOWLEDGMENTS

We are grateful to N. Kaiser for making the IMCAT package publicly available. We thank the anonymous referee for useful comments and important suggestions which greatly improved the quality of the manuscript. EM thanks Eran Ofek for his publicly available Matlab scripts. Work at Tel-Aviv University was supported by Israel Science Foundation grant 214/02 and supported in part by National Science Council of Taiwan under the grant NSC97-2112-M-001-020-MY3.

REFERENCES

- Adelman-McCarthy J. K., Agüeros M. A., Allam S. S., Allende Prieto C., Anderson K. S. J., Anderson S. F., Annis J., Bahcall N. A., et al., 2008, *ApJS*, 175, 297
- Bacon D. J., Massey R. J., Refregier A. R., Ellis R. S., 2003, *MNRAS*, 344, 673
- Benítez N., 2000, *ApJ*, 536, 571
- Bertin E., 2006, in *Astronomical Data Analysis Software and Systems XV*, Gabriel C., Arviset C., Ponz D., Enrique S., eds., pp. 112–+
- Bertin E., Arnouts S., 1996, *A&AS*, 117, 393
- Bolzonella M., Miralles J.-M., Pelló R., 2000, *A&A*, 363, 476
- Brammer G. B., Whitaker K. E., van Dokkum P. G., Marchesini D., Labbé I., Franx M., Kriek M., Quadri R. F., et al., 2009, *ApJ*, 706, L173
- Broadhurst T., Benítez N., Coe D., Sharon K., Zekser K., White R., Ford H., Bouwens R., et al., 2005, *ApJ*, 621, 53
- Broadhurst T. J., Taylor A. N., Peacock J. A., 1995, *ApJ*, 438, 49
- Brown M. L., Ade P., Bock J., Bowden M., Cahill G., Castro P. G., Church S., Culverhouse T., et al., 2009, *ApJ*, 705, 978
- Brown M. L., Taylor A. N., Bacon D. J., Gray M. E., Dye S., Meisenheimer K., Wolf C., 2003, *MNRAS*, 341, 100
- Capak P., Aussel H., Ajiki M., McCracken H. J., Mobasher B., Scoville N., Shopbell P., Taniguchi Y., et al., 2007, *ApJS*, 172, 99
- Coe D., Benítez N., Sánchez S. F., Jee M., Bouwens R., Ford H., 2006, *AJ*, 132, 926
- Fioc M., Rocca-Volmerange B., 1997, *A&A*, 326, 950
- Gilmore J., Natarajan P., 2009, *MNRAS*, 396, 354
- Grazian A., Fontana A., de Santis C., Nonino M., Salimbeni S., Giallongo E., Cristiani S., Gallozzi S., et al., 2006, *A&A*, 449, 951
- Heymans C., Van Waerbeke L., Bacon D., Berge J., Bernstein G., Bertin E., Bridle S., Brown M. L., et al., 2006, *MNRAS*, 368, 1323
- Ilbert O., Capak P., Salvato M., Aussel H., McCracken H. J., Sanders D. B., Scoville N., Kartaltepe J., et al., 2009, *ApJ*, 690, 1236
- Inada N., Oguri M., Pindor B., Hennawi J. F., Chiu K., Zheng W., Ichikawa S.-I., Gregg M. D., et al., 2003, *Nature*, 426, 810
- Jain B., Connolly A., Takada M., 2007, *J. Cosmology Astropart. Phys.*, 3, 13
- Jain B., Taylor A., 2003, *Physical Review Letters*, 91, 141302
- Kaiser N., Squires G., Broadhurst T., 1995, *ApJ*, 449, 460
- Kitching T. D., Heavens A. F., Taylor A. N., Brown M. L., Meisenheimer K., Wolf C., Gray M. E., Bacon D. J., 2007, *MNRAS*, 376, 771
- Kotulla R., Fritze U., Weilbacher P., Anders P., 2009, *MNRAS*, 396, 462
- Massey R., Rhodes J., Leauthaud A., Capak P., Ellis R., Koekemoer A., Réfrégier A., Scoville N., et al., 2007, *ApJS*, 172, 239
- Medezinski E., Broadhurst T., Umetsu K., Coe D., Benítez N., Ford H., Rephaeli Y., Arimoto N., et al., 2007, *ApJ*, 663, 717
- Medezinski E., Broadhurst T., Umetsu K., Oguri M., Rephaeli Y., Benítez N., 2010, *MNRAS*, 405, 257
- Miyazaki S., Komiyama Y., Sekiguchi M., Okamura S., Doi M., Furusawa H., Hamabe M., Imi K., et al., 2002, *PASJ*, 54, 833
- Oguri M., Inada N., Keeton C. R., Pindor B., Hennawi J. F., Gregg M. D., Becker R. H., Chiu K., et al., 2004, *ApJ*, 605, 78
- Perlmutter S., Aldering G., Goldhaber G., Knop R. A., Nugent P., Castro P. G., Deustua S., Fabbro S., et al., 1999, *ApJ*, 517, 565
- Riess A. G., Filippenko A. V., Challis P., Clocchiatti A., Diercks A., Garnavich P. M., Gilliland R. L., Hogan C. J., et al., 1998, *AJ*, 116, 1009
- Santini P., Fontana A., Grazian A., Salimbeni S., Fiore F., Fontanot F., Boutsia K., Castellano M., et al., 2009, *A&A*, 504, 751
- Schrabback T., Hartlap J., Joachimi B., Kilbinger M., Simon P., Benabed K., Bradač M., Eifler T., et al., 2010, *A&A*, 516, A63+
- Seitz C., Schneider P., 1997, *A&A*, 318, 687
- Sharon K., Ofek E. O., Smith G. P., Broadhurst T., Maoz D., Kochanek C. S., Oguri M., Suto Y., et al., 2005, *ApJ*, 629, L73
- Soucail G., Kneib J., Golse G., 2004, *A&A*, 417, L33
- Spergel D. N., Bean R., Doré O., Nolte M. R., Bennett C. L., Dunkley J., Hinshaw G., Jarosik N., et al., 2007, *ApJS*, 170, 377
- Steidel C. C., Adelberger K. L., Giavalisco M., Dickinson M., Pettini M., 1999, *ApJ*, 519, 1
- Taylor A. N., Bacon D. J., Gray M. E., Wolf C., Meisenheimer K., Dye S., Borch A., Kleinheinrich M., et al., 2004, *MNRAS*, 353, 1176
- Taylor A. N., Kitching T. D., Bacon D. J., Heavens A. F., 2007, *MNRAS*, 374, 1377
- Umetsu K., Birkinshaw M., Liu G.-C., Wu J.-H. P., Medezinski E., Broadhurst T., Lemze D., Zitrin A., et al., 2009, *ApJ*, 694, 1643
- Umetsu K., Broadhurst T., 2008, *ApJ*, 684, 177
- Umetsu K., Medezinski E., Broadhurst T., Zitrin A., Okabe N., Hsieh B., Molnar S. M., 2010, *ApJ*, 714, 1470
- Wittman D., Tyson J. A., Margoniner V. E., Cohen J. G., Dell’Antonio I. P., 2001, *ApJ*, 557, L89
- Yagi M., Kashikawa N., Sekiguchi M., Doi M., Yasuda N., Shimasaku K., Okamura S., 2002, *AJ*, 123, 66
- Zacharias N., Monet D. G., Levine S. E., Urban S. E., Gaume R., Wycoff G. L., 2004, in *Bulletin of the American Astronomical Society*, Vol. 36, *Bulletin of the American Astronomical Society*, pp. 1418–+
- Zitrin A., Broadhurst T., 2009, *ApJ*, 703, L132
- Zitrin A., Broadhurst T., Rephaeli Y., Sadeh S., 2009a, *ApJ*, 707, L102
- Zitrin A., Broadhurst T., Umetsu K., Coe D., Benítez N., Ascaso B., Bradley L., Ford H., et al., 2009b, *MNRAS*, 396, 1985